Spectral correction algorithm for multispectral CdTe x-ray detectors

Dreier, Erik Schou; Kehres, Jan; Khalil, Mohamad; Busi, Matteo; Gu, Yun; Feidenhans'l, Robert Krarup; Olsen, Ulrik Lund

Published in:
Optical Engineering

Link to article, DOI:
10.1117/1.OE.57.5.054117

Publication date:
2018

Document Version
Publisher's PDF, also known as Version of record

Optical Engineering

OpticalEngineering.SPIEDigitalLibrary.org

Spectral correction algorithm for multispectral CdTe x-ray detectors

Erik Schou Dreier
Jan Kehres
Mohamad Khalil
Matteo Busi
Yun Gu
Robert Feidenhans'l
Ulrik Lund Olsen

SPIE.

Erik Schou Dreier, Jan Kehres, Mohamad Khalil, Matteo Busi, Yun Gu, Robert Feidenhans'l, Ulrik Lund Olsen, "Spectral correction algorithm for multispectral CdTe x-ray detectors," *Opt. Eng.* **57**(5), 054117 (2018), doi: 10.1117/1.OE.57.5.054117.

Optical Engineering 57(5), 054117 (May 2018)

Spectral correction algorithm for multispectral CdTe x-ray detectors

Erik Schou Dreier,[a,*] Jan Kehres,[b] Mohamad Khalil,[b] Matteo Busi,[b] Yun Gu,[b] Robert Feidenhans'l,[c] and Ulrik Lund Olsen[b]
[a]University of Copenhagen, Niels Bohr Institute, Copenhagen, Denmark
[b]Technical University of Denmark, Department of Physics, Lyngby, Denmark
[c]European XFEL GmbH, Schenefeld, Germany

Abstract. Compared to the dual-energy scintillator detectors widely used today, energy-resolved photon-counting x-ray detectors show the potential to improve material identification in various radiography and tomography applications used for industrial and security purposes. However, detector effects, such as charge sharing and photon pileup, distort the measured spectra in pixelated, photon-counting detectors operating under high flux. These effects result in a significant performance degradation of the detectors when used for material identification where accurate spectral measurements are required. We have developed a semianalytical, postdata acquisition, computational algorithm that corrects the measured attenuation curve for severe spectral distortions caused by the detector. The calibration of the algorithm is based on simple attenuation measurements of commercially available materials using standard laboratory sources, enabling the algorithm to be used in any x-ray setup. The algorithm is developed for correcting spectral data acquired with the MultiX ME100 CdTe x-ray detector but could be adapted with small adjustments to other photon-counting, energy-resolved detectors with CdTe sensors. The validation of the algorithm has been done using experimental data acquired with both a standard laboratory source and synchrotron radiation. The experiments show that the algorithm is fast, reliable at x-ray flux up to 5 Mph/s/mm^2 and greatly improves the accuracy of the measured spectrally resolved linear attenuation, making the algorithm useful for both security and industrial applications where photon-counting detectors are used. [DOI: 10.1117/1.OE.57.5.054117]

Keywords: CdTe detectors; compensation of spectral distortions; photon-counting detector; MultiX ME100 detector; pulse pileup correction; charge sharing correction.

Paper 180289P received Feb. 23, 2018; accepted for publication May 9, 2018; published online May 25, 2018.

1 Introduction

Photon-counting x-ray detectors with spectroscopic properties (multispectral x-ray detectors) and CdTe sensors show great potential for improving material identification in hard x-ray applications,[1] and methods to utilize the increased information obtained with multispectral data are still under development.[2,3] This has led to a large interest in multispectral detectors within security[4,5] and medical applications.[6–8] These applications typically require a large field of view, a difficulty which has been addressed by the development of multilevel polycrystalline (thin film) detectors[9,10] as well as detectors with a line array of multiple single crystals.[8,11]

However, detector effects, such as charge sharing and pulse pileup, severely distort the measured spectrum of multispectral detectors.[6] Spectral distortion might be mitigated through the implementation of advanced digital pulse processing techniques in the field-programmable gate array.[12,13] However, the recorded spectra from commercially available multispectral detectors are still severely distorted.

A common spectral correction approach is to empirically determine a photon flux density-dependent fitting function, which translates each energy bin's measured signal into a corrected signal.[14] Unfortunately, this method typically corrects the count rate of each energy bin independently of the others, whereas the spectral distortion, such as pulse pileup,[15] effect on an energy bin's count rate is largely correlated with the count rate in all other energy bins. Therefore, the empirical fitting function-based approach is not ideal for applications, such as luggage screening, where large variations in density and effective atomic number among the measured objects result in large variation in the measured x-ray spectra. An alternative method is to correct the recorded spectra using analytical or empirical models of the individual spectral distorting effects. Comprehensive models of the spectral distortion in multispectral x-ray detectors have been proposed numerous times,[16–19] and algorithms that correct the measured spectrum for the specific effects of pulse pileup and escape peaks based on analytical models are already in use.[15,20] Furthermore, it has been shown that using a comprehensive model to add distortions to the expected x-ray spectrum improves the ability to estimate the thickness of attenuating materials in simulated experiments.[21]

In this paper, we present a comprehensive semianalytical correction algorithm (CA) that directly corrects recorded x-ray spectra for charge sharing, weighting potential (WP) cross talk, pulse pileup, incomplete charge collection (ICC), and x-ray fluorescence, with the purpose of improving the accuracy of the measured material x-ray attenuation coefficients. Our CA is designed with the primary scope to correct data acquired with the MultiX ME100 v2 CdTe

*Address all correspondence to: Erik Schou Dreier, E-mail: erik.dreier@nbi.ku.dk

0091-3286/2018/$25.00 © 2018 SPIE

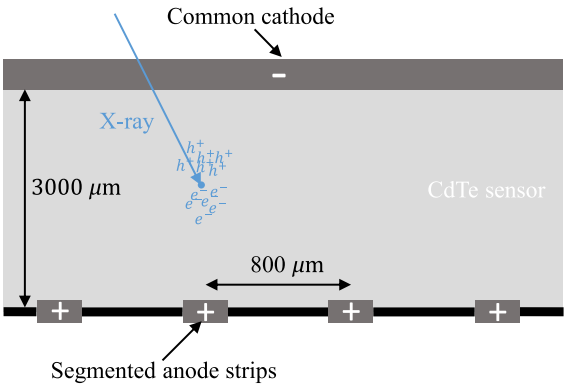

Fig. 1 Simplified layout of the MultiX detector.

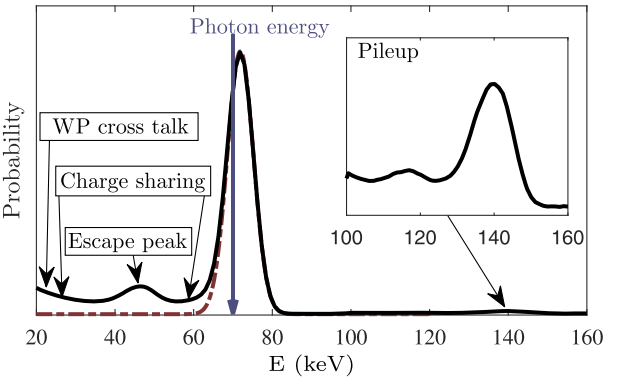

Fig. 2 The spectrum recorded with a MultiX ME100 v2 detector irradiated with a monochromatic x-ray beam of $E = 70$ keV. The "pileup box" shows a zoom-in on the pileup peak at double energy of the primary peak. The dashed red line shows the ideal response of the MultiX ME100 detector with a finite energy resolution. The primary peak's center is placed at slightly higher energy than the expected due to a slightly wrong energy calibration of the detector.

line array detector,[22] which suffers from severe spectral distortion.[11] However, the CA is based on spectral distortion models that with small adjustment could be applied to any pixelated, multispectral CdTe detector. We aim with this CA to gain the possibility to correct the measured x-ray attenuation coefficient for distorting effects in an efficient, fast, and reliable way making the CA applicable in nondestructive testing (NDT) and security applications.

The MultiX ME100 detector was chosen for this study, as it is suitable for security and NDT applications where a high flux, large field of view, and sensitivity for x-ray energies between 20 and 160 keV are required. Furthermore, the detector has shown to improve material identification as compared to conventional dual-energy sandwich detectors.[23–26] The MultiX's read-out architecture is constructed to perform well at high count rates (>1 Mph/s/mm^2) and is capable of reconstructing the measured x-ray spectra in up to 256 energy bins.[12,27] The detector has a 3-mm-thick CdTe sensor with a collective cathode on the photons' incident side of the sensor and a segmented anode on the backside as shown in Fig. 1. A single MultiX detector has 128 pixels with a pitch of 800 μm and is made up of an array of 4 sensor crystals with each 32 pixels. The detectors can further be daisy chained in up to 20 modules forming a more than 200-cm-long detector array.

In the rest of the paper, we will first introduce our CA in Sec. 2. In Sec. 3, we validate and adjust the CA's individual correction models based on experimental data from a monochromatic synchrotron source; next, we will show how the CA is calibrated using laboratory experiments in Sec. 4. Finally, we will validate the effectiveness of the full CA in Sec. 5, before discussing in Sec. 6 and concluding in Sec. 7, on our work.

2 Correction Algorithm for Spectral Distortion

The spectral response of multispectral, pixelated, CdTe detectors is typically severely distorted by a range of effects, as illustrated by the MultiX detector's recorded spectrum when irradiated by a monochromatic beam in Fig. 2. To correct for the spectral distortion, we follow the method proposed by Cammin et al.[18] and separate our distortion models into flux-dependent and flux-independent models. In our CA, we first correct the spectrum for the flux-independent phenomena, such as charge sharing, WP cross talk, etc. Next, we correct for the pulse pileup and then ICC, which as we shall show later is clearly flux dependent. Last, we recalibrate each pixel's energy scale. In the rest of this section, the models constituting our CA are presented.

2.1 *Flux-Independent Correction—The Simulated Detector Response Matrix*

Our CA aims to correct the spectrum for the following flux-independent effects:[15,16,28]

- X-ray fluorescence: Due to the high photon energy of the K-shell fluorescence in CdTe, the self-absorption length is so large that it is probable for the fluorescence photons to escape into a neighboring pixel or even to escape the detector's sensor crystal altogether. When such an escape occurs, the incident photon is registered by the detector at an energy lowered by the energy of the fluorescence photon.
- Charge sharing: If an x-ray photon is absorbed close to a pixel border, the created electron charge cloud can split onto both pixels resulting in the absorbed photon being counted as two photons with lower energy. This gives rise to a broad continuum of counts with an energy lower than the actual photon energy.
- WP cross talk: Charge carriers that are solely recorded by one pixel-anode might still induce a signal in the neighboring anode. The effect is seen as an upturn in the spectrum at low energies (seen at $E < 30$ keV in Fig. 2).
- Other flux-independent effects: In addition to the WP cross talk, charge sharing, and escape peaks, other effects, such as Compton scattering of the incident photon in the sensor crystal and electronic noise,[27] can contribute to the background.

To perform a fast correction of these flux-independent effects, we create an inverse detector response matrix $\mathbf{M}_C$ of dimension $E_b \times E_b$, where E_b is the number of energy bins. When $\mathbf{M}_C$ is applied to a raw spectrum from N pixels, described as a matrix $\mathbf{I}_R$ of dimension $E_b \times N$, it results in the corrected spectrum for each pixel described by the matrix

$$\mathbf{I}_C = \mathbf{M}_C \cdot \mathbf{I}_R. \tag{1}$$

The inverse response matrix is found from a simplified simulation of the detector's response to x-ray irradiation. To simplify the simulation, the WP cross talk, charge sharing, and electronic noise/Compton scattering are calculated independently. Therefore, this approach results in three response matrices, which all show to be numerically invertible, and hence

$$\mathbf{M}_C = (\mathbf{D}_C \cdot \mathbf{D}_E \cdot \mathbf{D}_{\mathrm{WP}})^{-1}, \tag{2}$$

where $\mathbf{D}_C$, $\mathbf{D}_E$, and $\mathbf{D}_{\mathrm{WP}}$ are the detector response matrices due to charge sharing, electron noise and Compton scattering, and WP cross talk, respectively. Applying $\mathbf{M}_C$ according to Eq. (1), we first correct for the WP cross talk, then the electronic noise and Compton scattering, and last the charge sharing. The order was chosen to remove the low-energy distortion effects before correcting for charge sharing.

The full detector response matrix is computed through a Monte Carlo simulation of a single pixel's response to x-ray irradiation as function of position and energy of the incoming photon. The simulation computes x-ray fluorescence before calculating $\mathbf{D}_C$, $\mathbf{D}_E$, and $\mathbf{D}_{\mathrm{WP}}$ matrices independently.

The amount of charge shared between two pixels is calculated by assuming that the excited charge clouds have a Gaussian charge density distribution.[29] The charge cloud width σ_t at the anode is calculated taking the charge diffusion and the charge repulsion perpendicular to the electric field into account. Combined with the initial width of the excited charge cloud σ_i that is assumed to be 5 μm,[30] the total width of the electron cloud is given as

$$\sigma_t = \sqrt{2\frac{k_B T z d}{qU} + \left(\frac{zdNq}{10\pi\epsilon U}\right)\frac{1}{\sqrt{5}\sigma_i} + \sigma_i^2}, \tag{3}$$

where z is the electron cloud position above the anode, d is the depth of the crystal layer, and U is the bias voltage. The number of charges per photon is given as $N = E_e/\Delta_E$, where $\Delta_E = 4.43$ eV/ehp[31] is the energy per electron–hole pair (ehp) for CdTe and E_e is the energy deposited in the detector by the absorbed photon.

The amount of WP cross talk between the irradiated and neighboring pixel is based on the model described by Guerra et al.,[16] which assumes that the charge cloud has no geometric expansion. In the model, the anode is assumed rectangular with a and b being the width and length of the anode, respectively.

Both Compton scattering and electronic noise should contribute with a small signal in the low-energy part of the spectrum, which should increase with incoming photon energy. The detector response matrix, $\mathbf{D}_E$, that accounts for these two effects is calculated through a simplified model that is based on synchrotron experiments as described in Sec. 3.

In the simulation of the MultiX ME100 detector, the pixel is set to an area of 0.8×0.8 mm^2, with an active crystal layer thickness of 3 mm,[23] and a bias voltage of around 1200 V.[27] The energy range of the simulation is set to 20 to 160 keV corresponding to the energy bin interval of the MultiX ME100. The WP cross talk model's anode size parameters a and b are found from finding the best correction of the experimental data as described in Sec. 4. The combined response matrix $\mathbf{M}_C = \mathbf{D}_{\mathrm{WP}} \cdot \mathbf{D}_E \cdot \mathbf{D}_C$ is shown in Fig. 3.

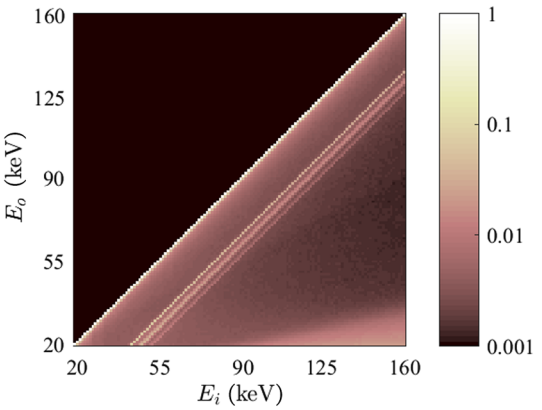

Fig. 3 The simulated detector response matrix $\mathbf{D}_{\mathrm{WP}} \cdot \mathbf{D}_E \cdot \mathbf{D}_C$ as function of the incoming photon's energy E_i and the recorded energy E_o. The color scale shows the probability density of recording an event.

A more detailed description of the simulation and models can be found in Appendix A.

2.2 *Incomplete Charge Collection*

CdTe suffers from a large difference in the drift mobility of the electrons, $\mu_e = 1000$ cm^2/V, and holes, $\mu_h = 80$ cm^2/V.[31] To mitigate this problem, CdTe detectors typically take advantage of the small pixel effect, where the ICC is reduced by having the segmented anode pads significantly smaller than the depth of the detector crystal. This minimizes the holes contribution to the signal formation and, thereby, reduces the problem with ICC due to trapping of the slow holes.[32] Despite this, ICC still occurs resulting in photons being registered with lower energy than their actual one, causing a skew of the measured spectrum toward lower energy.[20] Furthermore, effects such as polarization from the buildup of charge over time will cause ICC as well.[33]

A common description of the ICC's effect on the recorded spectrum of an incoming photon with energy E_i comes from modeling it as[20]

$$S(E) = H(E) * K(E), \tag{4}$$

where $H(E)$ is a Gaussian function with mean equal to E_i and standard deviation equal to the spectral resolution of the detector. The convolution kernel is given as

$$K_{E_k}(E) = \left[\mathrm{erf}\left(\frac{E - E_k}{\sqrt{2}\sigma_{\mathrm{ICC}}}\right) + 1\right] \cdot \chi_0(E), \tag{5}$$

for which $E_k = \mathrm{median}(E)$ and $\chi_0(E) = \begin{cases} 1, & \text{if } E \le E_k \\ 0 & \text{Otherwise} \end{cases}$.

σ_{ICC} is a scalable constant found empirically from laboratory data, which we show in Sec. 3, and is flux dependent.

2.3 *Pulse Pileup Model*

Pulse pileup occurs due to the overlapping of electrical pulses generated in an anode by two photons arriving close in time in the same pixel. To correct for the effect of pulse pileup, we use the iterative model developed by Plagnard,[15]

as described in Appendix B. To account for the photon flux-dependent pileup probability, Plagnard uses a coefficient C_{PU}, which is determined by the operator. We instead propose an automatic fitting approach using the attenuation curve of aluminum to find C_{PU}. This approach is described in Sec. 4.

2.4 *Energy Calibration*

Fluctuations in the measured energy in the order of a few keV might occur between the pixels in the detector. To calibrate the detector for these variations, the spectrum of the radioactive isotope ^{57}Co was measured. For each pixel's measured spectrum, the peak center of the primary and secondary radiation lines of the isotope as well as the escape peaks can be found. By fitting a first-degree polynomial to the expected peak centers as a function of the measured peak centers, a conversion from the measured to the actual energy is found.

3 Synchrotron Experiments

The synchrotron experiments presented in this paper were conducted at the materials science beamline ID11 at the European Synchrotron Radiation Facility (ESRF). The aim of these experiments was to evaluate our models' prediction of the distorting effects. At the ID11 beamline, the MultiX ME100 detector's response to monochromatic x-ray radiation was measured at 8 different energies between 24 and 138 keV. The x-ray energy selection was provided by double-bent crystal monochromator operating in horizontal focusing Laue geometry. The MultiX detector was mounted on the camera stage in the EH3 hutch allowing for movement in the plane perpendicular to the beam. The beam size onto the detector was controlled using slits placed just in front of the EH3 sample stage, and the beam position on the detector was changed by moving the detector stage. To obtain a reference measurement to validate the energy of the monochromatic beam, a high-energy resolution Amptek XR100T CdTe PIN-diode detector was mounted on the sample stage. The monochromatic x-ray beam's energy distribution FWHM was determined to be below the 1.4-keV resolution limit of the Amptek detector. An x-ray beam energy distribution FWHM of 1.4 keV is well below the energy resolution of the MultiX detector (estimated to be 8 keV at $E = 122$ keV at fluxes below 2 Mph/s/mm^2).[27]

3.1 *Evaluating the Flux-Independent Models*

The MultiX ME100's response to a monochromatic x-ray beam of FWHM 5×5 μm^2 was measured as a function of beam position on the detector. The detector was moved parallel and perpendicular to the pixel array in steps of $\sim$20 μm. The scan parallel to the pixel array was made across two pixels starting from approximately the center of a pixel. The detector response was measured for 2 s at each beam position before moving the detector. In Fig. 4(a), the result of a scan at $E = 123$ keV can be seen as a function of beam position and recorded energy.

The detector response of different sensor crystals (each MultiX module has 128 pixels and uses 4 tiled CdTe crystals) was evaluated by making an additional scan across 50 pixels with 5 steps per pixel. The result of this scan showed no significant change in spectral behavior among the individual pixels, except for the 2 pixels closest to the MultiX sensor crystal borders. In these border pixels, the count efficiency drops and the measured spectrum is pushed toward lower energies. In the rest of this paper, we, therefore, exclude the spectra of the 2 pixels closest to the crystal borders from all experiments and expect each of the remaining pixels to behave alike.

To evaluate the flux-independent models of our CA, the pencil beam position scan was simulated by adjusting the position and area of the simulated incoming photons' position in accordance with the experiment. The result of the simulation is shown in Fig. 4(b).

In the center of the pixel ($x \sim 585$ μm), the experimental result in Fig. 4(a) shows a tail on the primary peak ($E \sim 123$ keV) toward lower energy and a small signal at $E < 50$ keV.

To incorporate the low-energy signal in the center of the pixel in the simulation, an additional noise term was required on top of charge sharing, WP cross talk, and x-ray fluorescence. As explained in Sec. 2, we assume that Compton scattering of the incoming photon in the sensor crystal as well as electronic noise can generate such a low-energy noise signal. Hence, the new noise term was collected in the response matrix $\mathbf{D}_E$. To simulate this effect, a very simple model

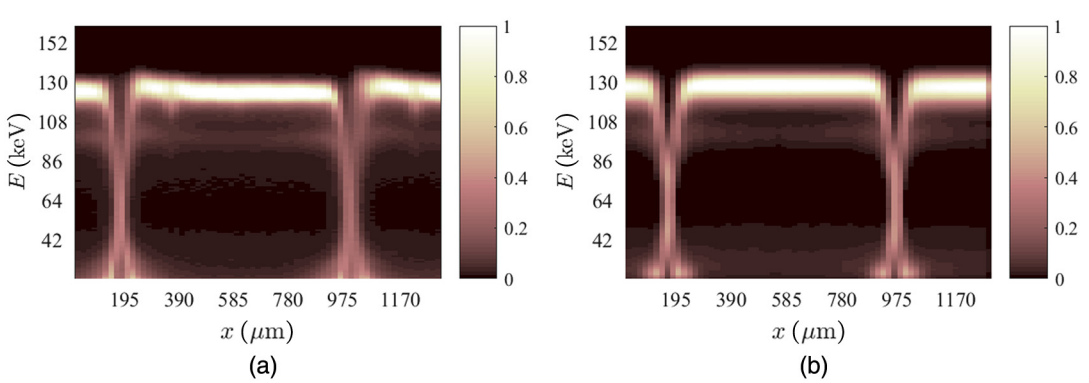

Fig. 4 The (a) measured and (b) simulated detector response as function of readout energy and the position of the monochromatic ($E = 123$ keV) pencil beam on the detector. Both simulation and experiment show two pixel border crossings positioned at $x \approx 195$ and 975 μm. The simulated spectra were convolved with K_{E_k} described in Eq. (5) to account for the peak broadening and ICC. Both color scales are normalized to peak intensity.

was developed. The effect is assumed to be position independent and modeled by including a probability, P_n, for a charge signal to be recorded subsequent to a photon being recorded. The charge signal is assumed to be a fraction of the charge deposited by the absorbed photon, with a probability distribution modeled as Gaussian with mean μ_n and width σ_n. This is done to ensure that the noise contribution's importance will increase as the photon energy increases, providing that the amount of excited charge is proportional to the absorbed energy.

The low-energy noise seen in the center of the pixel in the simulated detector response in Fig. 4(b) solely comes from the detector response matrix $\mathbf{D}_E$. We notice that the simulation overestimates the low-energy signal slightly. The value of the parameters used for this model was found from laboratory experiments as shown in Sec. 4.

The tailing effect on the primary peak shown in Fig. 4(a) was included in the simulated spectrum by convolving the simulation result with the kernel K_{E_k}, described in Eq. (5). We notice that this model slightly underestimates the extent of the primary peak's energy tail as best seen from the difference between estimated and measured signal at $E \sim 80$ keV.

Figure 4 clearly shows the incorrect recorded energy around the pixel borders due to the effect of charge sharing, x-ray fluorescence, and WP cross talk. To evaluate the simulation models, we take the sum of the measured intensity of each pixel at each position, as shown in Fig. 5(a) for a monochromatic beam with $E = 123$ keV. For each border, the cross talk intensity, i.e., the intensity that is measured in the neighboring pixel to the one being irradiated, can be fitted with a double Gaussian distribution

$$g(x) = A_{g,1} \exp\left[\frac{(x-\mu_g)^2}{2\sigma_{g,1}^2}\right] + A_{g,2} \exp\left[\frac{(x-\mu_g)^2}{2\sigma_{g,2}^2}\right], \quad (6)$$

where the identical mean of the two Gaussian distributions μ_g is forced equal to the border position, and the height $A_{g,i}$ and width $\sigma_{g,i}$ are scalable fit variables. Similar fits were made for all eight energies for both of the two pixel borders reached in the parallel scans. The resulting widths $\sigma_{g,1}$ and $\sigma_{g,2}$ are shown for all energies and both borders in Fig. 5(b).

Figure 5(b) shows that the narrowest width of the Gaussian distribution $\sigma_{g,2}$ corresponds to the expected charge cloud size estimated from Eq. (3). The broad distribution $\sigma_{g,1}$ seems to be well accounted for by the simulated extent of the WP cross talk and fluorescence photons into the neighboring pixel. However, a discrepancy is seen at energies below the K-edge of cadmium ($E_{\mathrm{Cd}} = 26.7$ keV), where a long ranged cross talk of the order of 100 μm is seen in the experimental result but not refound in the simulated model.

As a final remark, we notice that the read-out energy of the primary peak in Fig. 4(a) is shifted slightly across the pixel as function of position, an observation that was reproduced in the neighboring pixels as well. This effect was found to become more pronounced at low energies but was not studied further.

3.2 *Flux-Dependent ICC*

The flux dependence of the MultiX detector was evaluated using flux scans at ID11 at different energies with a beam positioned at the center of a pixel. The flux scans were made through increasing the beam cross section by opening the slits in steps from 5×5 μm^2 to 65×65 μm^2. In Fig. 6(a), the result of such a scan is shown for a $E = 50$ keV monochromatic beam. From the position scans and simulation in Fig. 4, it was estimated that the cross talk among pixels did not extend far enough into the pixel to affect the flux dependence measurement, and that Compton scattering and electronic noise were negligible at incoming photons with $E < 90$ keV. In Fig. 6(a), the escape peak around $E = 25$ keV and the main pulse pileup peak at $E = 100$ keV are clearly seen. As expected, the relative amplitude of the main peak decreases as the pileup peak increases with flux.

In Fig. 6(a), the spectra are clearly distorted toward lower energies as the beam flux is increased. This resembles the expected distortion from ICC, described by Eq. (4), and it, therefore, seems that the ICC increases with flux. To evaluate this effect, the main peak of the raw spectrum was fitted with $S(E)$ described by Eq. (4), with σ_{ICC} being the only parameter allowed to change with increased flux. Due to the possibility of a highly noisy spectrum, deconvolving the image with the full $S(E)$ is numerically difficult due to the Gaussian function. However, it is possible to correct for the skewness of the peak by deconvolving each spectrum with $K(E_e)$ using the σ_{ICC} found from fitting $S(E)$. The deconvolution was done using MATLAB™'s[34] built-in

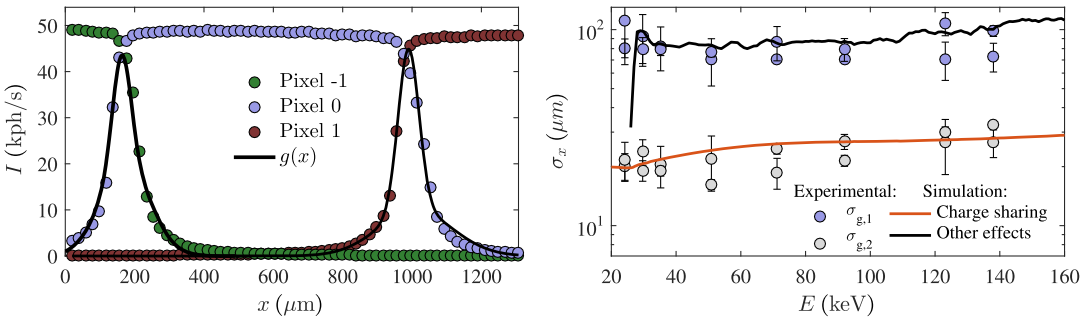

Fig. 5 Evaluating the spatial extent of the pixel cross talk. (a) The summed measured intensity of each pixel (numbered −1, 0, and 1) as function of the incoming monochromatic ($E = 123$ keV) pencil beam's position fitted with $g(x)$, Eq. (6), around the pixel borders ($x \approx 200$ and 975 μm). (b) The obtained widths $\sigma_{g,1}$ and $\sigma_{g,2}$ of $g(x)$ plotted as function of incoming photon energy with the theoretical estimated charge cloud width (charge sharing), and the width of the WP cross talk's and x-ray fluorescence's intensity distribution (other effects) superimposed.

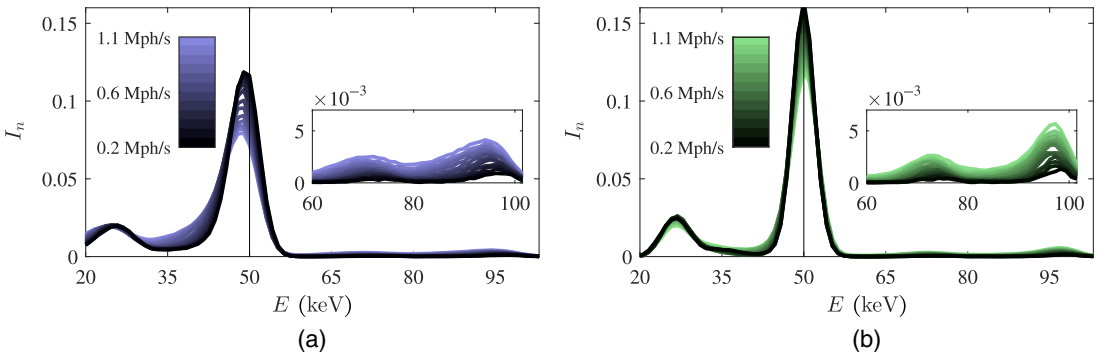

Fig. 6 Deconvolving the measured spectrum at different detector count rates (color scale) with a $K(E_e)$ kernel presented in Eq. (5). (a) The raw normalized spectrum I_n was fitted with $S(E)$, Eq. (4), from which the parameter σ_{ICC} was acquired. (b) Using the found σ_{ICC} for each spectrum, the spectral skew effect described by $K(E_e)$ can be removed through a Richardson–Lucy deconvolution and a corrected spectrum obtained. The inset box shows a zoom-in on the pileup peaks at $E = [60,100]$ keV.

Richardson–Lucy algorithm.[35,36] The result of a Richardson–Lucy deconvolution is shown in Fig. 6(b). The deconvolution works well in correcting the spectra for the peak skew as function of flux, as seen when comparing Figs. 6(a) and 6(b). To utilize this deconvolution in a correction model, a lookup table of σ_{ICC} as function of flux needs to be made. In Sec. 4, we show how this is done using the attenuation of aluminum measured with a laboratory source.

4 Laboratory Experiments

In this section, we show the laboratory measurements necessary for calibrating our CA. The x-ray laboratory experiments presented in this paper were performed in the energy dispersive x-ray diffraction (EDXRD) setup at Technical University of Denmark (DTU),[37] with a COMET MXR-160HP/11 tube that has a tungsten (W) target and a COMET MXR generator capable of operating with a voltage up to 160 kVp at a power of up to 1800 W. The x-ray flux from the source was adjusted by changing the current. Tungsten slits were used to collimate the beam and reduce the sample and environment scattering background. The scattering background from the sample in this setup was estimated to be insignificant using the simulation model described in Ref. 38.

4.1 *Optimizing the Flux-Independent Models*

The CA's flux-independent models, collected in the response matrix $\mathbf{M}_C$ presented in Eq. (2), were optimized through a simple experiment. A series of x-ray spectra were acquired by changing the source voltage and inserting different filters to attenuate the beam. For all generated spectra, the x-ray flux was kept low ($\Phi < 0.4$ Mph/s/mm^2) to minimize the effect of the flux-dependent distortions. As a reference, the same spectra were measured with the Amptek XR100T CdTe PIN-diode detector (at a count rate <10 kph/s), which due to its high-energy resolution at low count rates can be assumed to describe the true x-ray spectra. The flux-independent models contain the scalable parameters a and b in Eq. (18), as well as μ_n, σ_n, and P_n, which are used for the low-energy noise response matrix $\mathbf{D}_E$. The optimal flux-independent correction of the MultiX data was found by varying these parameters in a randomized search for the minimum χ^2 value between the corrected MultiX data and the Amptek reference data.

The best correction of the MultiX data was found for $a = b = 0.72$ mm; $P_n = 22.2\%$, $\mu_n = 0.174E_i$, and $\sigma_n = 0.2E_i$, where E_i is the simulated incoming photon energy. At these values, the low-energy noise model predicts that a recordable signal ($E > 20$ keV) from this contribution first exceeds 10% of the primary signal at incoming photon energies above 90 keV.

Two corrected spectra are shown in Fig. 7. The Amptek spectrum is convoluted with a Gaussian kernel of width $\sigma = 4$ keV corresponding to the upper energy resolution of the MultiX ME100 detector, to compare the two detectors' recorded spectra. As shown in the figure, the correction showed good correspondence to the reference measurement. Qualitatively, this was the case for all spectra we tested.

4.2 *Optimizing the Flux-Dependent Coefficients*

The proposed flux-dependent coefficients C_{PU} and σ_{ICC} presented in Eqs. (5) and (19), respectively, need to be identified from experiments. To do this, we used a measurement of the linear attenuation coefficient given as

$$\mu(E) = -\frac{1}{x}\log\left[\frac{I(E)}{I_0(E)}\right], \tag{7}$$

where $I(E)$ is the measured x-ray spectrum of the x-ray beam that has passed through the material, $I_0(E)$ is the incident spectrum measured at the detector (flat field), and x is the thickness of the material. Since the linear attenuation coefficient is a material constant independent of thickness, it can be used as a reference measure of how well the CA performs.

The measurement of the linear attenuation was done by placing aluminum plates of six different thicknesses between the detector and the source. An example of the result from such an experiment is shown in Fig. 8. The experiment was repeated for four different incident fluxes. By adjusting C_{PU} and σ_{ICC} for both $I(E)$ and $I_0(E)$ spectra, we obtain a best-fit between any measured attenuation curve of aluminum and the theoretically expected curve,[39] using the χ^2 value as a measure of the quality of the fit. The measured linear attenuation is fitted to the theoretical for the n different thicknesses of aluminum for each flat field flux. By doing so, n C_{PU} and σ_{ICC} values are obtained for both the flat field and attenuated

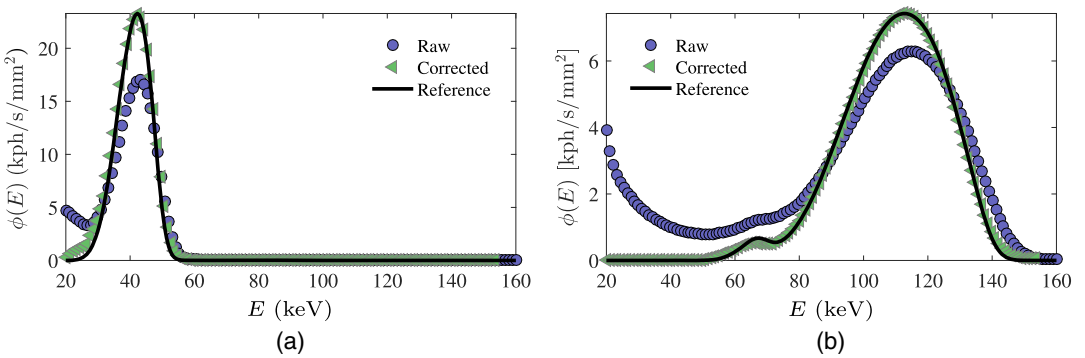

Fig. 7 Comparison between a MultiX spectrum corrected with the CA (corrected), a raw MultiX spectrum (raw), and a reference spectrum obtained with Amptek XR100 (reference). The reference spectrum is scaled to fit the corrected data. The shown spectra were obtained using (a) a filter of 19.9-mm aluminum at a source voltage of $U = 50$ kV and (b) 5.96-mm copper and 0.2-mm tantalum at $U = 140$ kV.

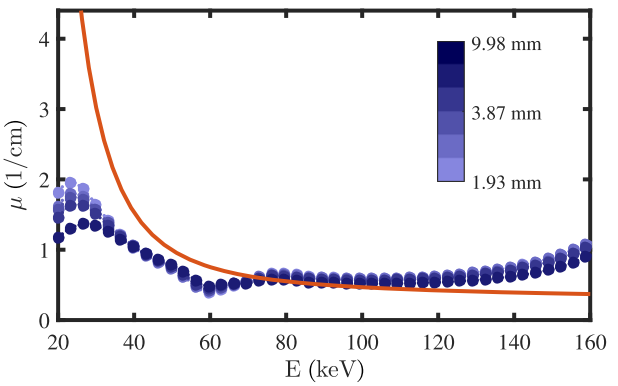

Fig. 8 Comparison between the measured linear attention curves (blue circles highlight every third point) of aluminum at different thicknesses given in the color scale, and the theoretical expected[39] (solid red line). The flat field flux was 3.7 Mph/s/mm^2.

spectra. Afterward, the n different flat field C_{PU} and σ_{ICC} are averaged. The linear attenuation fitting is then repeated, but this time using the average C_{PU} and σ_{ICC} to correct the flat field spectrum as an initial guess. Repeating this procedure ensures that the flat field spectrum correction is similar for all thicknesses.

In Fig. 9, the C_{PU} and σ_{ICC} values that result in the best-fit between measured and theoretical linear attenuation coefficient are shown for 28 spectra from 4 sets of measurement, each containing a flat field spectrum $I_0(E)$ and 6 attenuated spectra $I(E)$. The C_{PU} and σ_{ICC} coefficients are fitted with a first-order polynomial. The polynomials are used to generate fast lookup tables for correcting the spectra.

5 Final Validation of the Full Correction Algorithm

To test the full CA, a second dataset was acquired in the EDXRD setup at DTU, containing the measured linear attenuation coefficient of different thicknesses of PVC, aluminum, copper, and tantalum at different flat field fluxes. By applying the CA to the flat field and attenuated spectra and calculating the linear attenuation coefficient from these, we obtain the corrected linear attenuation curve. The measured and the corrected linear attenuation curves can be seen for a flat field flux $\Phi_0 = 4.7$ Mph/s/mm^2 in Fig. 10. In the figure, it can be seen that correcting the attenuation curve for spectral distortion improves the similarity between the measured and the theoretical expected attenuation. Particularly, at $E < 50$ keV, the CA clearly gives a much better fit between theory and data. It has to be noted that the corrected curves do not extend to 20 keV for the heavier elements,

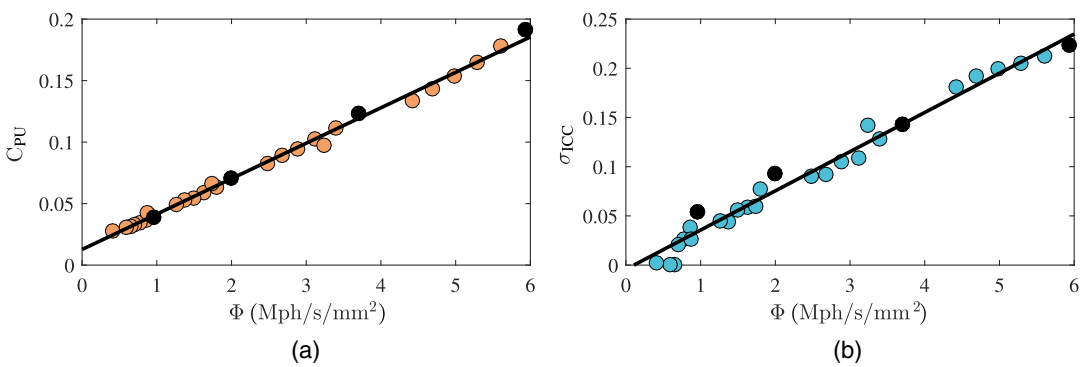

Fig. 9 (a) Pileup, C_{PU} and (b) ICC, σ_{ICC} coefficients found from fitting the linear attenuation curve of aluminum measured with the MultiX ME100 to the theoretical expected. Each point represents a corrected spectrum. The colored circles represent the correction coefficient used for the 4×6 attenuated spectra from the 6 different thicknesses of aluminum at 4 different flat field fluxes. The black circles represent the coefficients used for the 4 flat field spectra. The black lines are the C_{PU} and σ_{ICC} lookup tables, explained in the main text.

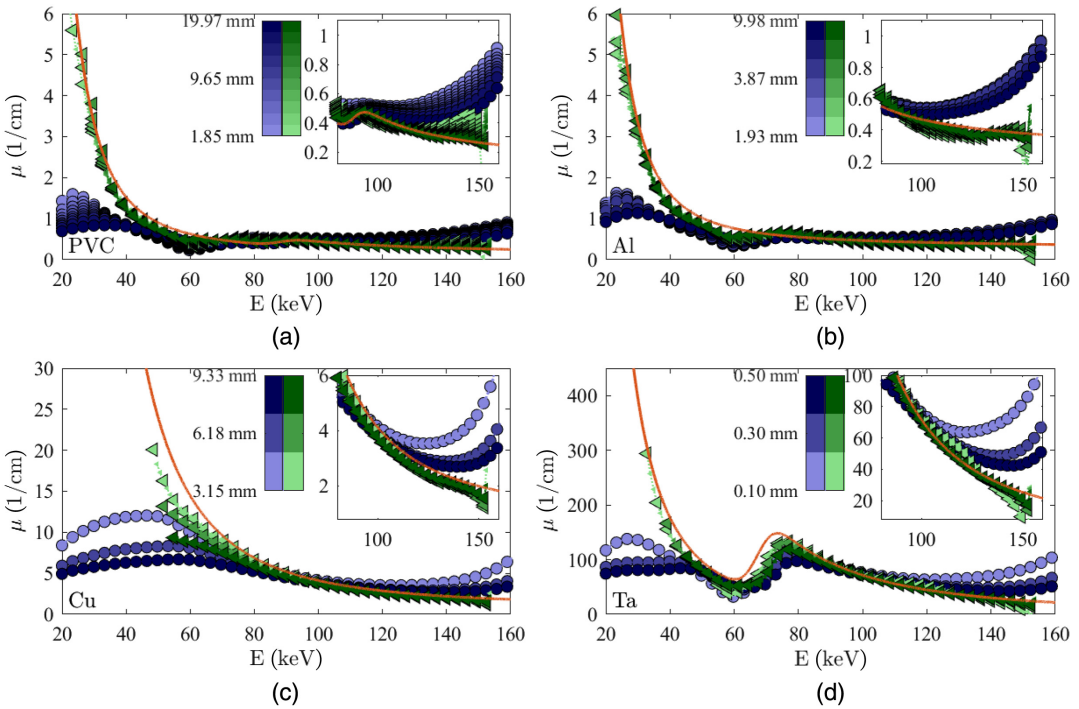

Fig. 10 Comparison between raw (blue circles) and corrected (green triangles) attention curves of (a) PVC, (b) aluminum, (c) copper, and (d) tantalum at a flat field flux of $\Phi_0 = 4.7$ Mph/s/mm^2. Every fifth data point is highlighted with a large marker. The color scales of the raw (left) and corrected (right) attenuation curves show the thickness of the measured material. The theoretical curves (solid red) are convoluted with a Gaussian kernel with $\sigma = 4$ keV.

copper and tantalum. This is due to the signal-to-noise ratio converging to zero when the corrected energy bins contain close to zero photons.

The performance of the CA is quantified by calculating the weighted correlation coefficient among the different curves. To account for statistical noise, the correlation weights were set equal to the inverse variance of the raw attenuation curve as measured by the variation between different pixels' data for both the raw and the corrected data. In Fig. 11, each material's average weighted self-correlation coefficient among the N attenuation curves is shown as function of flat field flux. Using Fisher's transform to compute the average correlation,[40] we define the average weighted self-correlation as $\overline{r}_{1,j} = \tanh\left[\frac{1}{N-1}\sum_{j=2}^{N}\tanh^{-1}(r_{1,j})\right]$, where $r_{1,j}$ is the correlation coefficient between the thinnest sheet of material, 1, and the j'th thickest. Furthermore, the figure also shows the average correlation coefficient between theory $\overline{r}_{t,j} = \tanh\left[\frac{1}{N}\sum_{j=1}^{N}\tanh^{-1}(r_{t,j})\right]$ and the j'th thickest sheet. To compare raw and corrected data equally, in both cases, the correlation coefficient is only calculated in the energy range, where the corrected data contain noninfinite values due to zero counts in the attenuated spectra. As can be seen from the figure, the average correlation coefficient of the corrected data with theory decreases very little across the full range of flat field flux, whereas the correlation between the raw curves and theory falls with increasing flux. Further, the average correlation coefficient between theoretical attenuation and the attenuation curves from the corrected data remains above, or in the case of tantalum close to, 0.95 even at high flux. Likewise, the average self-correlation coefficient of the corrected attenuation curves remains above 0.95, whereas this is only the case for aluminum in the raw dataset.

6 Discussion

The CA presented in this paper is made to correct the x-ray attenuation coefficient measured with the pixelated, multispectral detectors for multiple spectral distorting effects. The CA corrects the attenuation curve by correcting the measured flat field and attenuated x-ray spectra with the use semianalytical interpretations based on the physical origin of the different effects. Figure 10 clearly shows that the CA qualitatively improves the linear attenuation compared to theory. In particular, the CA improves the low-energy part of the attenuation, which is typically important for material identification.

In Fig. 11, we quantified that the CA improves the measured attenuation curve, both in respect to the correlation between measured and theoretical expected, but more importantly, the self-correlation between curves of different thicknesses. The latter means that the CA gives a more consistent result of the linear attenuation coefficient between different material thicknesses compared to the raw data. Furthermore, the results shown in Fig. 11 show that the CA improves the measured attenuation curves across a range of thicknesses, effective atomic number, and flat field fluxes up to at least 5 Mph/s/mm^2. This shows that the algorithm is reliable in security and other NDT applications, where unknown and largely varying samples are measured.

6.1 *Possible Improvements of the CA*

The individual models of our CA can easily be adjusted independently of each other if better models are found for any of

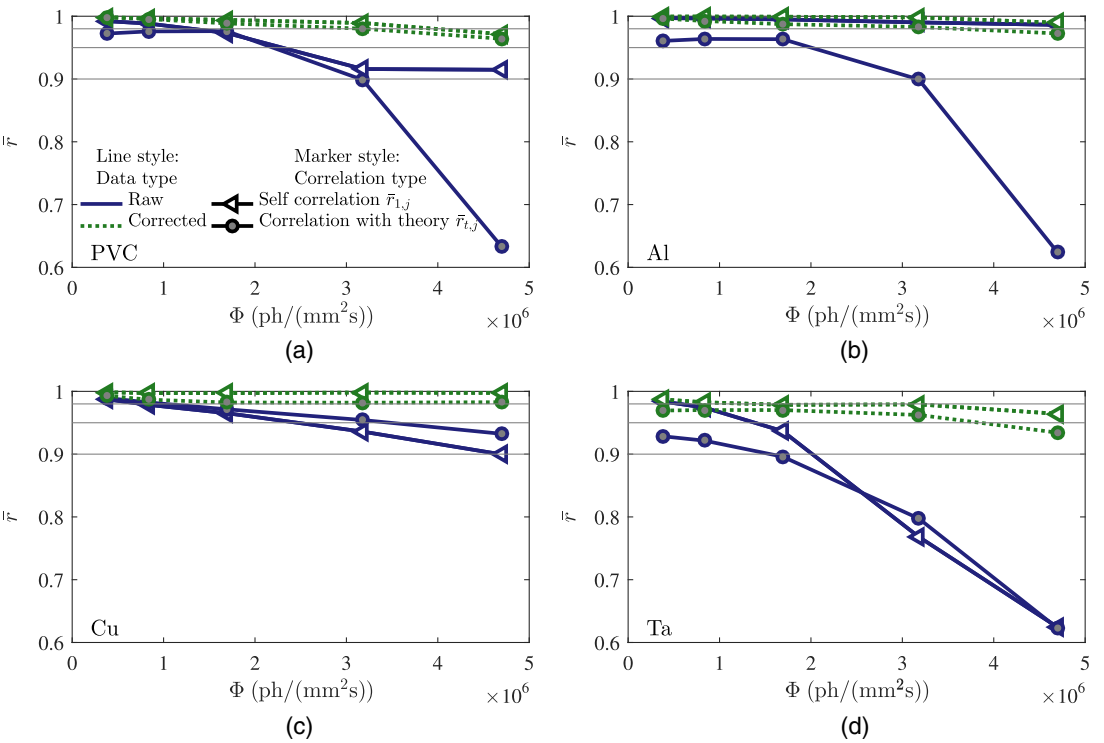

Fig. 11 The average weighted correlation coefficient as function of flat field flux, for both corrected and raw linear attenuation curves of (a) PVC, (b) aluminum, (c) copper, and (d) tantalum. The figure shows both the average weighted self-correlation coefficient between measured attenuation curves from different thicknesses of material and the average weighted correlation coefficient between the curves and the theoretical expected. Both correlation coefficients are explained in the main text. The gray straight lines mark $\bar{r} = 0.9$, $\bar{r} = 0.95$, and $\bar{r} = 0.98$.

the effects. Even though the CA clearly improves the measured attenuation curve, several of the CA's models do not fully describe the measured distortions and could be improved.

A significant distortion that is not correct by our CA is the clear drop in attenuation coefficient around $E = 59$ keV and the smaller drop around $E = 65$ keV observed in both Figs. 8 and 10. The two coincide with the tungsten K_α and K_β peaks ($E_\alpha = 59.3$ keV and $E_\beta = 67.2$ keV, respectively)[41] from the source. We expect that the drop in attenuation is due to a distortion of the tungsten peaks from the flux-dependent ICC and a general decrease of energy resolution with photon flux.[27]

Figure 4 showed that the expected MultiX detector response function could not fully account the distortion's effect in the center of the pixel. A better model than our simple empirical model of the Compton scattering in the sensor crystal and electronic noise could be added to the CA to improve the modeling of these effects. Such a new model might be part of the MultiX detector simulation and include the angular cross section of the Compton scattering and a model of the readout electronics. It is likely that Compton scattering could contribute with a loss of recorded energy of the incoming photon, resembling an ICC in addition to the recorded low-energy Compton electron signal.

The CA presented in this paper corrects the pixels spectra independently, assuming that the incident flux on two neighboring pixels is similar. The model could be improved by taking the neighboring pixels' intensity into account in cross talk models. In addition to this, the CA could be improved by developing a correction method applicable to the pixels surrounding the sensor crystal borders. In the present model designed for the MultiX ME100 detector, 4 pixels are removed for every crystal (32 pixels) corresponding to 12.4%.

6.2 *Computation Time*

The CA is based on MATLAB™ R2016a, and an extensive optimization of computing time has not yet been performed. The algorithm takes advantages of MATLAB™'s fast matrix multiplication, meaning that correcting multiple spectra together is faster than correcting them individually. At present, using a standard laptop equipped with an Intel i7-6600U quad-core CPUs at 2.60 GHz, the CA is capable of correcting the spectra of a full MultiX ME100 detector (128 pixels) in 50 ± 0.5 ms whereas a single pixel correction takes 7 ± 1 ms. It is in particular the two flux-dependent, ICC and the pileup correction, models that add to the computation time. The ICC and pileup models take around 42.7% and 42.3% of the computational time, respectively. There is, therefore, a great potential to reduce the computation time by optimizing these two flux-dependent models of the CA.

Furthermore, the present algorithm could easily be run in parallel, correcting each pixel independently, which without any further optimization would reduce the correction time to that of a single pixel, i.e., 7 ± 1 ms. By correcting a batch of acquisition frames, e.g., 50 frames of each 1 ms, the correction time could be reduced to <0.5 ms per frame. This means

that the present CA, if run in parallel, could correct the measured spectra in real time even at a frame rate of 1 ms and, hence, be used in applications where material identification needs to be fast, e.g., luggage screening in airports.

6.3 *Setup Compatibility*

The CA presented in this paper is optimized and tested for the MultiX ME100 v2, but the models are directly convertible to any CdTe line array detector and could with small adjustments be used for two-dimensional (2-D) CdTe flat panel or even CZT detectors. The calibration of the CA only requires a measurement of the attenuation coefficient of a well-defined material, such as aluminum, at different thicknesses and at different flat field fluxes. This means that the CA can easily be used in other experimental setups. In addition to this, an energy calibration measurement might be needed. This can be done with x-ray fluorescence from metals or a well-known radioactive isotope source.

7 Conclusion

We have in this paper shown an effective algorithm for correcting the material-dependent x-ray attenuation for effects, such as charge sharing, WP cross talk, pulse pileup, etc. The presented algorithm is designed and tested on data acquired with the MultiX ME100 but could be adapted to other formats of pixelated CdTe and CZT detectors with small adjustments. Using synchrotron and laboratory sources, the different correction models have been verified and the algorithm has been tested. The results from calculating the linear attenuation curves from the corrected flat field and attenuated spectra indicate that a better correspondence to data from theoretical reference tables is possible if the CA is applied to the raw data. Furthermore, the corrected measurements give significantly more consistent data, which should enable a more reliable material identification in various applications. The algorithm is applicable in any setup requiring only a few calibration measurements using easily accessible materials. The present algorithm is reasonably fast, correcting 128 pixels' spectra (contain 128 energy bins) in 50 ± 0.5 ms, and it could easily be improved by one or two orders of magnitude, making it useful in application, such as luggage screening in airports and other high-throughput NDT setups.

Appendix A: Simulating the Response Matrix

In the following, the simulation of the detector response due to escape peaks, charge sharing, electronic noise and Compton scattering, and WP cross talk is presented in detail. The models are designed to account for one-dimensional (1-D) pixelarray detector but could be extended to 2-D flat panel detectors.

The simulation is based on a single-photon Monte Carlo simulation of a pixel irradiated with x-rays. The photon's absorption position as a function of depth in the crystal is simulated according to the probability distribution given by the expected attenuation of CdTe.[39]

A.1 Escape Peak and X-Ray Fluorescence

The effect of escape peaks is taken into account by including x-ray fluorescence in the simulation. X-ray fluorescence occurs when the energy of the photon is larger than the K 1s shell binding energy ($E_{\mathrm{Cd}} = 26.711$ keV for Cd and $E_{\mathrm{Te}} = 31.814$ keV for Te[42]). The refilling of the K-shell results the emission of a photon as either K_α or K_β fluorescence, with a probability given by the fluorescence yield. The energy of the fluorescence lines is for cadmium $E_\alpha = 23.2$ keV and $E_\beta = 26.1$ keV and tellurium $E_\alpha = 27.5$ keV and $E_\beta = 31.0$ keV.[42] In the simulation, each absorbed photon with energy E_i and absorption location $\mathbf{r}_i$ has a probability to emit a K_α or K_β fluorescence photon from either Cd or Te with energy E_f governed by the value of E_i compared to the energy of the K 1s shell of Cd and Te:

- $E_i < E_{\mathrm{Cd}}$: No fluorescence photon is emitted.
- $E_{\mathrm{Cd}} < E_i < E_{\mathrm{Te}}$: A fluorescence photon is emitted with an 84% probability equaling the fluorescence yield of cadmium.[43] The energy E_f of the created fluorescence photon is set to either $E_f = 23.2$ keV ($P_f = 0.18$) or $E_f = 26.1$ keV ($P_f = 0.82$), where P_f is the probability of each energy.
- $E_i > E_{\mathrm{Te}}$: A fluorescence photon is created with probability of 85.8% equaling the average fluorescence yield of cadmium and tellurium.[43] The energy of the created fluorescence photon is set to $E_f = 23.2$ keV ($P_f = 0.09$), $E_f = 26.1$ keV ($P_f = 0.41$), $E_f = 27.5$ keV ($P_f = 0.09$), or $E_f = 31.0$ keV ($P_f = 0.41$).

The K_α or K_β fluorescence probability for the cadmium and tellurium used above is calculated according to the values reported in Ref. 43. In the simulation, the fluorescence photons are emitted in a random direction and absorbed at $\mathbf{r}_f$. The fluorescence photon's travel distance before absorption $|\mathbf{r}_f - \mathbf{r}_i|$ is simulated according to the probability distribution function given by the attenuation in CdTe. If a fluorescence photon is emitted, the energy deposited at $\mathbf{r}_i$ is set to $E_d = E_i - E_f$ and the remaining energy E_f is absorbed in $\mathbf{r}_f$, else $E_d = E_i$. If $\mathbf{r}_f$ lies outside the detector volume, the energy contained in the fluorescence photon is removed from the simulation and, hence, not detected. This creates an escape peak.

In the simulation, the initially absorbed photon and the fluorescence photon will be recorded at the same time, meaning that the recorded energy will be the sum of the energy deposited in a pixel from both photons.

A.2 Charge Sharing

The final $\mathbf{D}_C$, $\mathbf{D}_{\mathrm{WP}}$, and $\mathbf{D}_N$ response matrices are calculated by making 2-D histograms of all simulated photons' recorded and their respective incoming energy. The calculation of charge sharing and WP cross talk both result in an amount of energy being recorded on the pixels neighboring the center pixel where the photon was initially absorbed. Energy recorded in a neighboring pixel will be included in the final response matrices, by including them as separate events in the histograms. In the following, the energy deposited in a location $\mathbf{r}_0 = (x_0, y_0, z_0)$ will be denoted E_0 (and is either $E_0 = E_d$ or $E_0 = E_f$). Pixelated, multispectral CdTe detectors typically have a segmented anode collecting the electrons responsible for the spatial resolution of the detector and a common cathode collecting the holes. Therefore, the charge sharing and WP cross talk are in the simulation

assumed to be coursed only by the drift of the excited electrons.

The amount of electrons shared between two pixels is calculated for each photon by assuming that the excited electron cloud is a 1-D Gaussian distribution parallel to the pixel array. In this model, the deposited energy recorded in the neighboring pixels to the "left" or "right" of the primary pixel is given by[29]

$$E_{\text{right}} = \frac{E_0}{2}\left[1 - \text{erf}\left(\frac{d_x/2 - x_0}{\sigma\sqrt{2}}\right)\right],$$
$$E_{\text{left}} = \frac{E_0}{2}\left[1 - \text{erf}\left(\frac{d_x/2 + x_0}{\sigma\sqrt{2}}\right)\right], \tag{8}$$

where d_x is the width of the pixel and σ is the standard deviation of the electron cloud distribution. The energy recorded in the center pixel is given by $E_{\text{center}} = E_0 - E_{\text{right}} - E_{\text{left}}$. It is noted that in the simulation $\mathbf{r}_0$ will be confined to the central pixel for the original absorbed photon, but in the case of fluorescence photon, it can be in either the left or right neighbor pixel. The electron cloud at the anode, where the electrons are recorded, is assumed to be given by

$$\sigma = \sqrt{\sigma_t^2 + \sigma_i^2}, \tag{9}$$

where $\sigma_i = 5\ \mu\text{m}$[30] is the initial width of the excited charge cloud and σ_t can be calculated from the diffusion equation

$$\sigma_t^2 = 2D\tau, \tag{10}$$

where D is the diffusion constant and τ is the charge carrier lifetime.[28] To include the charge repulsion in this model, an effective diffusion constant is used[30]

$$D_{\text{eff}} = D + \frac{1}{15}\left(\frac{3\mu_e N q}{4\pi\epsilon}\right)\frac{1}{\sqrt{5}\sigma_i}, \tag{11}$$

where μ_e is the electron mobility, q is the elementary charge, and ϵ is the permittivity. The number of charges per photon is given by $N = E_e/\Delta_E$, where $\Delta_E = 4.43\ \text{eV/ehp}$[31] is the energy per ehp for CdTe and E_e is the energy deposited in the detector by the absorbed photon. The additional contribution to the charge cloud distribution due to reabsorbed fluorescence photons creating two cloud centers is thereby not taken into account. This choice was made to simplify calculations of the charge sharing effect.

By combining Eqs. (10) and (11), we obtain an expression for the cloud width due to repulsion and diffusion

$$\sigma_t = \sqrt{2\tau D + \frac{2\tau}{15}\left(\frac{3\mu_e N q}{4\pi\epsilon}\right)\frac{1}{\sqrt{5}\sigma_i}}. \tag{12}$$

According to the Einstein relation $D = \frac{\mu_e k_B T}{q}$, where T is the temperature and k_B is the Boltzmann's constant. Assuming parallel plate electrodes with bias voltage U, we can rewrite the drift time in terms of detector depth d and interaction point compared to the anode z, such that $\mu_e\tau = \frac{zd}{U}$.[44] By combining the latter with Eqs. (9) and (12), we find

$$\sigma_t = \sqrt{2\frac{k_B T z d}{qU} + \left(\frac{zdNq}{10\pi\epsilon U}\right)\frac{1}{\sqrt{5}\sigma_i} + \sigma_i^2}. \tag{13}$$

A.3 WP Cross Talk

According to the description presented in Ref. 12, the WP cross talk originates from current induced in the neighboring pixels to the pixel where the excited charge cloud is moving. The induced current in neighboring pixels integrates to zero along the charge clouds drift path; however, if the induced current becomes large enough, it might still trigger a signal in the detector. The induced charge $Q(\mathbf{r})$ on an electrode due to moving charges in the active detector volume is described by the Shockley–Ramo theorem[28,45,46]

$$Q(\mathbf{r}) = N_0 \cdot q \cdot \phi(\mathbf{r}), \tag{14}$$

where N_0 is the number of charge carrier, q is the charge of the carriers, and $\phi(\mathbf{r})$ is the WP. The WP cross talk induced from each photon is in our simulation modeled by rewriting Eq. (14) into

$$\Delta E = E_0 \cdot \Delta\phi_j(\mathbf{r}_0), \tag{15}$$

where ΔE is the recorded energy from the charge induced in pixel j, and E_0 is the energy of the photon absorbed in pixel $j+1$, and $\Delta\phi_j$ is the difference in the WP of pixel j from the start of the charge drift path at the absorption point $\mathbf{r}_0$ to the point where the maximum charge is induced (i.e., where the current reverses on the j pixel). The model is a simplification as it assumes a point shape charge cloud containing all charge induced from a photon.

A simple model of the WP $\phi_j(\mathbf{r})$ is described in Ref. 16, where it is assumed that the detector consists of two infinite parallel plates. This model is taken as a simple approximation of the WP cross talk in the MultiX ME100, and it is repeated here for the ease of the reader. The model uses the method of mirror charges, where the WP can be described by an infinite sum of charge mirrors

$$\phi_j(\mathbf{r}) = \sum_{k=-\infty}^{\infty} \phi_0(x, y, z - 2kd, a, b), \tag{16}$$

where d is the depth of the CdTe crystal, and a and b are the dimensions of the anode pad, which is assumed rectangular. Under this assumption, the mirror potential is given by

$$\phi_0(x, y, z) = \frac{1}{2\pi}\left[\arctan\left(\frac{(a-\xi)(b-\eta)}{z\sqrt{(a-\xi)^2 + (b-\eta)^2 + z^2}}\right)\right.$$
$$+ \arctan\left(\frac{(a-\xi)\eta}{z\sqrt{(a-\xi)^2 + \eta^2 + z^2}}\right)$$
$$+ \arctan\left(\frac{\xi(a-\xi)}{z\sqrt{(\xi^2 + (b-\eta)^2 + z^2}}\right)$$
$$\left. + \arctan\left(\frac{\xi\eta}{z\sqrt{\xi^2 + \eta^2 + z^2}}\right)\right], \tag{17}$$

with

$$\xi = \frac{(x - x_1)(x_2 - x_1) + (y - y_1)(y_2 - y_1)}{a},$$
$$\eta = \frac{-(x - x_1)(y_2 - y_1) + (y - y_1)(x_2 - x_1)}{b}. \quad (18)$$

In the above, the corners of the anode are placed at (x_i, y_i) for $i = 1 \ldots 4$ and x, y, z, are the simulated interaction points of the charge above pixel $j - 1$ with respect to the center of anode j. A way to determine a and b is described in Sec. 4 in the main paper. Equation (16) should be evaluated as an infinite sum, however, in the simulation, the sum is only evaluated in $k = [-2,2]$, as it has been shown to be a reasonable approximation.[47]

A.4 Compton Scattering and Electrical Noise

As explained in the main text, the detector response due to Compton scatter and electronic noise, contained in the response matrix $\mathbf{D}_E$, is calculated through a simplified model.

In the model, we assume that either the Compton electron or the scattered photon is recorded in the same pixel, i.e., the recorded energy will be equal to the incoming photon's energy or the scattered photon escapes the detector leaving only the Compton electron to be recorded. There is a finite probability that the Compton electron and the scattered photon will be recorded in different pixels, resulting in the scattered photon being recorded with energy lower than its incident when entering the crystal. This effect is not included in the model. However, this effect resembles that of the ICC, which is corrected for by the ICC model, and, hence, mitigates the effect of Compton scattering on the primary recorded photon energy.

Both the Compton scattering cross section and Compton edge (maximum energy transferred to the scattered electron) increase with energy.[28] The Compton edge becomes larger than 20 keV at photon incoming energies $E_i > 82$ keV. Hence, the low-energy spectrum is only affected by the photon above 82 keV. In addition to this, electronic noise, which arises as example from fluctuations in the leakage current, can contribute with a signal at low energies as well. To include these effects, we assume that the absorption of a photon would generate an electronic noise or Compton scattering charge signal with a probability P_n, described by a distribution modeled as Gaussian with mean μ_n and width σ_n. As the noise is added as a fraction of the original charge deposited in the detector, the noise contribution's importance will increase as the photon energy increases, since the amount of charge excited by the absorbed photon energy is proportional to the absorbed energy. Thereby, the noise term will have almost no importance at low energy where it will create a signal below the detection limit of the MultiX ME100 of 20 keV. The exact values of the parameters used to describe the noise term were found empirically as described in the experimental section.

Appendix B: Pulse Pileup Model

To correct for pulse pileup, we use the method developed by Plagnard,[15] which we present below for the ease of the reader. The model is based on the assumption that two photons with energy E_1 and E_2 will be counted as one with the combined energy of the two $E_t = E_1 + E_2$, if the time between the two is small enough. The effect of the pulse pile up on the measured spectrum $I_R(E)$ is described by the pileup spectrum $I_{PU}(E_{nx})$. The pileup correction model needs to calculate $I_{PU}(E_{nx})$ for all values of E_n and E_x, with E_n and E_x being the center energy of the MultiX ME100's n and x energy bin, respectively. For each n, the pileup spectrum is calculated for the whole range of x by

$$I_{PU}(E_{nx}) = \frac{I_R(E_n)}{\sum_e \overline{I}_R(E_e)} \cdot C_{PU} \cdot \overline{I}_R(E_x). \quad (19)$$

Afterward, the obtained spectrum $I_{PU}(E)$ is subtracted from the raw spectrum, and the summed contribution is added to $I_C(E_n)$ of the n energy bin to obtain the corrected spectrum

$$I_C(E) = I_R(E) - I_{PU}(E),$$
$$I_C(E_n) = I_C(E_n) + \sum_e I_{PU}(E_e). \quad (20)$$

At this point, n is increased and the procedure is repeated. Plagnard lets the coefficient C_{PU} in Eq. (19) be determined by the operator.

Acknowledgments

The authors would like to thank Exruptive for financing the ESRF beam time, through the initiative LINX (Linking Industry with Neutrons and X-rays) funded by Innovations fund Denmark. Furthermore, we thank Jon Wright from ID-11 for assistance during the beam time. The authors acknowledge Innovation Fund Denmark for financing this work. Preliminary results of this study have been presented at the SPIE Optical Engineering + Applications Conference on Radiation Detectors in Medicine, Industry, and National Security XVIII (2017) and published in the conference proceedings.[48]

References

1. G. Beldjoudi et al., "Multidimensional data processing methods for material discrimination using an ideal x-ray spectrometric photon counting detector," *IEEE Trans. Nucl. Sci.* **58**(6), 3190–3203 (2011).
2. Y. Yuan, B. Tracey, and E. Miller, "Robust x-ray based material identification using multi-energy sinogram decomposition," *Proc. SPIE* **9847**, 98470V (2016).
3. N. Kimoto et al., "Development of a novel method based on a photon counting technique with the aim of precise material identification in clinical x-ray diagnosis," *Proc. SPIE* **10132**, 1013239 (2017).
4. V. Rebuffel et al., "New perspectives of x-ray techniques for explosive detection based on CdTe/CdZnTe spectrometric detectors," in *Proc. of the Int. Symp. on Digital Industrial Radiology and Computed Tomography*, Vol. 2 (2011).
5. L. Martin, "Enhanced information extraction in the multi-energy x-ray tomography for security," PhD Thesis, Boston University (2014).
6. K. Taguchi and J. S. Iwanczyk, "Vision 20/20: single photon counting x-ray detectors in medical imaging," *Med. Phys.* **40**, 100901 (2013).
7. N. Anderson and A. Butler, "Clinical applications of spectral molecular imaging: potential and challenges," *Contrast Media Mol. Imaging* **9**, 3–12 (2014).
8. P. Shikhaliev, "Soft tissue imaging with photon counting spectroscopic CT," *Phys. Med. Biol.* **60**, 2453–2474 (2015).
9. E. I. Parsai, D. Shvydka, and J. Kang, "Design and optimization of large area thin-film CdTe detector for radiation therapy imaging applications," *Med. Phys.* **37**(8), 3980–3994 (2010).
10. D. Shvydka, X. Jin, and E. I. Parsai, "Performance of large area thin-film CdTe detector in diagnostic x-ray imaging," *Int. J. Med. Phys. Clin. Eng. Radiat. Oncol.* **2**(3), 98–109 (2013).
11. E. S. Jimenez et al., "Developing imaging capabilities of multi-channel detectors comparable to traditional x-ray detector technology for industrial and security applications," *Proc. SPIE* **9969**, 99690A (2016).

12. A. Brambilla et al., "CdTe linear pixel x-ray detector with enhanced spectrometric performance for high flux x-ray imaging," *IEEE Trans. Nucl. Sci.* **59**(4), 1552–1558 (2012).
13. L. Abbene et al., "Digital fast pulse shape and height analysis on cadmiumzinctelluride arrays for high-flux energy-resolved x-ray imaging," *J. Synchrotron Radiat.* **25**, 257–271 (2018).
14. H. Ding and S. Molloi, "Image-based spectral distortion correction for photon-counting x-ray detectors," *Med. Phys.* **39**, 1864–1876 (2012).
15. J. Plagnard, "Comparison of measured and calculated spectra emitted by the x-ray tube used at the Gustave Roussy radiobiological service," *X-Ray Spectrom.* **43**, 298–304 (2014).
16. P. Guerra, A. Santos, and D. G. Darambara, "Development of a simplified simulation model for performance characterization of a pixellated CdZnTe multimodality imaging system," *Phys. Med. Biol.* **53**, 1099–1113 (2008).
17. J. C. Kim, W. R. Kaye, and Z. He, "Signal modeling of charge sharing effect in simple pixelated CdZnTe detector," *J. Korean Phys. Soc.* **64**, 1336–1345 (2014).
18. J. Cammin et al., "A cascaded model of spectral distortions due to spectral response effects and pulse pileup effects in a photon-counting x-ray detector for CT," *Med. Phys.* **41**(4), 041905 (2014).
19. J. E. Fernandez, V. Scot, and L. Sabbatucci, "A modeling tool for detector resolution and incomplete charge collection," *X-Ray Spectrom.* **44**, 177–182 (2015).
20. R. H. Redus et al., "Characterization of CdTe detectors for quantitative x-ray spectroscopy," *IEEE Trans. Nucl. Sci.* **56**, 2524–2532 (2009).
21. J. Cammin et al., "Evaluation of models of spectral distortions in photon-counting detectors for computed tomography," *J. Med. Imaging* **3**, 023503 (2016).
22. "Multix—x-ray spectrometry in transmission for security, food, recycling," http://www.multixdetection.com/ (26 April 2018).
23. A. Gorecki et al., "Comparing performances of a CdTe x-ray spectroscopic detector and an x-ray dual-energy sandwich detector," *J. Instrum.* **8**, P11011 (2013).
24. M. Kheirabadi et al., "Multispectral x-ray CT: multivariate statistical analysis for efficient reconstruction," *Proc. SPIE* **10391**, 1039113 (2017).
25. A. Brambilla et al., "Basis material decomposition method for material discrimination with a new spectrometric x-ray imaging detector," *J. Instrum.* **12**, P08014 (2017).
26. I. M. E. Fulladosa and P. Gou, "Effect of dry-cured ham composition on x-ray multi energy spectra," *Food Control* **70**, 41–47 (2016).
27. A. Brambilla et al., "Fast CdTe and CdZnTe semiconductor detector arrays for spectroscopic x-ray imaging," *IEEE Trans. Nucl. Sci.* **60**(1), 408–415 (2013).
28. G. F. Knoll, *Radiation Detection and Measurement*, 3rd ed., John Wiley and Sons, Inc., New York (1999).
29. X. Wang et al., "Micro CT with energy-resolved photon-counting detectors," *Phys. Med. Biol.* **56**, 2791–2816 (2011).
30. L. A. Hamel et al., "Optimization of single-sided charge-sharing strip detectors," in *IEEE Nuclear Science Symp. Conf. Record* (2006).
31. D. S. McGregor and H. Hermon, "Room-temperature compound semiconductor radiation detectors," *Nucl. Instrum. Methods Phys. Res. Sect. A* **395**, 101–124 (1997).
32. H. H. Barrett, J. D. Eskin, and H. B. Barber, "Charge transport in arrays of semiconductor gamma-ray detectors," *Phys. Rev. Lett.* **75**(1), 156–159 (1995).
33. H. Toyama et al., "Quantitative analysis of polarization phenomena in CdTe radiation detectors," *Jpn. J. Appl. Phys.* **45**(11), 8842–8847 (2006).
34. "MATLAB processing toolbox," The MathWorks, Natick, Massachusetts (2016).
35. D. S. C. Biggs and M. Andrews, "Acceleration of iterative image restoration algorithms," *Appl. Opt.* **36**(8), 1766–1775 (1997).
36. R. J. Hanisch, R. L. White, and R. L. Gilliland, "Deconvolution of Hubbles Space Telescope images and spectra," in *Deconvolution of Images and Spectra*, 2nd ed., P. A. Jansson, Ed., pp. 310–360, Academic Press, Inc., Orlando, Florida (1996).
37. J. Kehres, M. Lyksborg, and U. L. Olsen, "Threat detection of liquid explosives and precursors from their x-ray scattering pattern using energy dispersive detector technology," *Proc. SPIE* **10393**, 1039302 (2017).
38. M. Busi et al., "Simulation tools for scattering corrections in spectrally resolved x-ray computed tomography using McXtrace," *Opt. Eng.* **57**(3), 037105 (2018).
39. NIST, "X-ray form factor, attenuation, and scattering tables," http://physics.nist.gov/PhysRefData/FFast/html/form.html (6 August 2017).
40. D. M. Corey, W. P. Dunlap, and M. J. Burke, "Averaging correlations: expected values and bias in combined Pearson rs and Fisher's z transformations," *J. Gen. Psychol.* **125**(3), 245–261 (1998).
41. NIST, "X-ray transition energies by element," http://physics.nist.gov/PhysRefData/XrayTrans/Html/search.html (6 August 2017).
42. A. Thompson and D. Vaughan, *X-Ray Data Booklet*, Lawrence Berkeley National Laboratory, Berkeley, California (2009).
43. W. Bambynek et al., "X-ray fluorescence yields, Auger, and Coster–Kronig transition probabilities," *Rev. Mod. Phys.* **44**(4), 716–813 (1972).
44. K. Iniewski et al., "Modeling charge-sharing effects in pixellated CZT detectors," in *IEEE Nuclear Science Symp. Conf. Record* (2007).
45. W. Shockley, "Currents to conductors induced by a moving point charge," *J. Appl. Phys.* **9**, 635–636 (1938).
46. S. Ramo, "Currents induced by electron motion," *Proc. IRE* **27**(9), 584–585 (1939).
47. A. Castoldi, E. Gatti, and P. Rehak, "Three-dimensional analytical solution of the Laplace equation suitable for semiconductor detector design," *IEEE Trans. Nucl. Sci.* **43**(1), 256–265 (1996).
48. E. D. Christensen et al., "Spectral correction algorithm for multispectral CdTe x-ray detectors," *Proc. SPIE* **10393**, 103930H (2017).

Erik Schou Dreier is a PhD student at the Niels Bohr Institute, University of Copenhagen, Denmark. He received both his BS and MS degrees in physics from the University of Copenhagen in 2013 and 2016. His research is focused on finding possible new applications and characterization of innovative single-photon-counting x-ray detectors. He is a member of SPIE.

Jan Kehres is a research engineer at Technical University of Denmark (DTU) Physics, Kongens Lyngby, Denmark. He received his PhD in operando investigation of catalyst nanoparticles using x-ray scattering and continued in this field of research as a postdoctoral researcher. His current field of research is the application of energy-dispersive detectors for x-ray scattering and advanced imaging modalities with a focus on material identification of illicit materials for security applications.

Mohamad Khalil is a postdoctoral researcher at DTU, Kongens Lyngby, Denmark. He received his MS degree in high-energy physics from the University Paris Pierre et Marie Curie, Paris, France, in 2011 and his PhD from the University Paris Denis Diderot, Paris, France, and University of Ferrara, Ferrara, Italy, in December 2014.

Matteo Busi is a PhD student at DTU, Kongens Lyngby, Denmark. He received his BS degree in physics from the Universit degli Studi di Parma, Parma, Italy, and his MS degree in mathematics and physics from the Universitetet i Stavanger, Stavanger, Norway, in 2014 and 2016, respectively. He is a member of SPIE.

Yun Gu was a postdoctoral researcher at DTU, Kongens Lyngby, Denmark from 2014 to 2017. She received her PhD from the University of Copenhagen, Copenhagen, Denmark, for advanced structural characterization of organic films specializing in x-ray diffraction technologies, and her master's degree in physics from the University of Siegen, Siegen, Germany.

Robert Feidenhans'l received his master's degree in physics and his PhD both from the University of Aarhus in 1983 and 1986, respectively. He has worked at Ris National Laboratory from 1986 to 2005. In 2005, he became a professor at the Niels Bohr Institute, University of Copenhagen. In January 2017, he became the managing director of the European XFEL, Hamburg. He has been working in the field of x-ray synchrotron radiation and free electron lasers his entire career.

Ulrik Lund Olsen is a senior research engineer at DTU Physics since 2013. He was funded by Innovation Fund Denmark to develop applications using high flux multispectral x-ray detection technology, and currently, he is the project leader on CIL2018, a multidisciplinary effort made to reduce the human operator involvement by 50% for checked-in luggage. He was previously employed at National Laboratory RISØ, Denmark, as PhD candidate in 2005 and later postdoc working with developments of x-ray sensors.